






RESEARCH ARTICLE

10.1029/2022JA030887

Ionospheric Response to Solar EUV Radiation Variations Using GOLD Observations and the CTIPE Model

Rajesh Vaishnav¹ , Christoph Jacobi¹ , Jens Berdermann² , Erik Schmöller² ,
Hanna Dühren² , and Mihail Codrescu³

¹Leipzig Institute for Meteorology, Leipzig University, Leipzig, Germany, ²German Aerospace Center, Neustrelitz, Germany,

³Space Weather Prediction Centre, National Oceanic and Atmospheric Administration, Boulder, CO, USA

Key Points:

- Ionospheric-thermospheric parameters observed by Global-Scale Observations of the Limb and Disk (GOLD) ultraviolet imaging spectrograph are compared with Coupled Thermosphere Ionosphere Plasmasphere electrodynamics model simulations
- The delayed ionospheric response against the solar flux is less than 1 day at the time scale of the 27 days solar rotation period
- The integrated 1–45 nm solar energy flux values observed by GOLD correlate well with the F10.7 and EUV

Correspondence to:

R. Vaishnav,
rajesh_ishwardas.vaishnav@uni-leipzig.de

Citation:

Vaishnav, R., Jacobi, C., Berdermann, J., Schmöller, E., Dühren, H., & Codrescu, M. (2024). Ionospheric response to solar EUV radiation variations using GOLD observations and the CTIPE model. *Journal of Geophysical Research: Space Physics*, 129, e2022JA030887. <https://doi.org/10.1029/2022JA030887>

Received 1 AUG 2022

Accepted 6 DEC 2023

©2023. The Authors.

This is an open access article under the terms of the [Creative Commons Attribution License](https://creativecommons.org/licenses/by/4.0/), which permits use, distribution and reproduction in any medium, provided the original work is properly cited.

Abstract To understand the global response of thermospheric-ionospheric (TI) parameters to variations in solar irradiance measurements from the Global-Scale Observations of the Limb and Disk (GOLD) ultraviolet imaging spectrograph, solar radio flux F10.7, predictions from the Coupled Thermosphere Ionosphere Plasmasphere electrodynamics (CTIPE) model, and International Global Navigation Satellite System Service total electron content maps (TEC) have been used. Various parameters such as GOLD O/N_2 , O_2 , and the nighttime peak electron density (Nmax) have been compared with the CTIPE model simulations. The GOLD observed Nmax shows a number of significant features including a winter anomaly and an equatorial ionization anomaly. The comparison with solar proxies showed that the GOLD Q_{EUV} correlates very well with the EUV observations compared to the F10.7 index. The study also examined the relationship between the solar proxies and Nmax on different time scales and found that Nmax responded significantly to Q_{EUV} at both medium- and long-term timescales. Furthermore, a low correlation between Nmax in the equatorial region and solar proxies was found. A delayed ionospheric TEC response against solar flux variations within the 27-day solar rotation was investigated. This ionospheric delay of TEC with respect to solar flux was observed to be less than 1 day, which was reproduced in model simulations. The current study has shown that the GOLD observations can be used to investigate the delayed ionospheric response and to gain a better understanding of the influence of solar activity on the TI system.

1. Introduction

Solar extreme ultraviolet (EUV) and ultraviolet (UV) irradiance is the main source of energy for the Earth's thermosphere and ionosphere (TI). It heats, dissociates and ionizes the neutral constituents atomic oxygen O , molecular oxygen O_2 , and molecular nitrogen N_2 (Schunk & Nagy, 2009). The ionospheric plasma is controlled by photochemical processes (photodissociation, photoionization, and recombination), transport processes (the neutral wind and diffusion), and lower atmospheric forcings. However, due to the unstable and fluctuating ionization source, the Sun, the ionosphere varies on a variety of time scales, including hourly, daily, seasonal, 11-year, and transient variations (e.g., Lean et al., 2001; Ma et al., 2012; Min et al., 2009; Vaishnav et al., 2019). Furthermore, the variability of the ionosphere is also caused by the neutral atmosphere composition, solar wind and geomagnetic activity, and electrodynamics (Rishbeth & Mendillo, 2001).

The thermospheric O/N_2 ratio (the column density ratio of atomic oxygen to molecular nitrogen) is a key parameter in determining compositional changes during the daytime (Rishbeth, 1998) and specifically during a geomagnetic storm (Zhang, 2004). The F2 region electron density is controlled by several factors including photoionization of O , loss by recombination and transport processes. Recombination is significantly faster for molecular ions than for atomic ions; therefore, ion/electron loss rates increase as the molecular to atomic ion ratio increases. Strickland et al. (1995) demonstrated that the O/N_2 ratio is proportional to the OI 135.6 nm to Lyman-Birge-Hopfield (LBH) bands intensity ratio, referenced to an N_2 depth of 10^{17} cm⁻².

Seasonal variations in solar zenith angle and changes in thermospheric composition (O/N_2) induced by meridional wind cause seasonal variations in ionospheric parameters such as total electron content (TEC) and peak electron density of the F2 layer (NmF2 or Nmax) (Fuller-Rowell & Rees, 1983). These include the winter anomaly (Rishbeth, 1998), or the nighttime winter anomaly effect (Jakowski et al., 2015). Direct continuous measurements of solar EUV/UV flux have been available since the launch of the Thermosphere Ionosphere Mesosphere Energetics and Dynamics (TIMED) satellite (Woods, 2005). The solar EUV flux Q_{EUV} is the integrated solar energy flux below 45 nm (Strickland et al., 1995). Q_{EUV} has been used to study solar flares (Strickland et al., 2007).

In addition, several solar proxies are available, but they are not always well suited to indicate the solar EUV band (Laštovička, 2021), with the F10.7 index (Tapping, 2013) being the most widely used one (Dudok de Wit et al., 2009). Vaishnav et al. (2019) studied multiple solar proxies to investigate the variations on different timescales and found that He-II, followed by Mg-II, were the best of the 12 studied.

Fluctuations in solar activity, due to the quasi 27-day solar rotation, significantly modulate ionospheric parameters such as TEC and NmF2 (Kutiev et al., 2013). During the 27-day solar rotation period, the peak of ionospheric electron density lags the peak time of solar EUV flux, resulting in a delay of several hours to 2 days (so called delayed ionospheric response) (e.g., Jakowski et al., 1991; Afraimovich et al., 2008; Kutiev et al., 2013; Jacobi et al., 2016; Ren et al., 2019, 2020; Schmölter et al., 2018, 2020, 2021, 2022; Vaishnav et al., 2018, 2019, 2022, & references therein).

To explore the physical mechanism and improve our understanding of the delayed ionospheric response, coupled ionosphere-thermosphere models have been used (e.g., Ren et al., 2020; Schmölter et al., 2022; Vaishnav et al., 2018, 2022; Vaishnav, Jacobi, et al., 2021). Photoionization is dominant at the electron density peak (strongest EUV absorption and greater concentration of O and O^+). Photodissociation is dominant in the lower ionosphere (strongest UV absorption and largest concentration of O_2). Therefore, additional O is produced in the lower ionosphere, which in turn by transport (diffusion) contributes to an increase of O and O^+ at the F region peak, resulting in a delayed electron density response to the changes in the solar EUV flux. This has been successfully modeled (Schmölter et al., 2022) and confirmed by observations (Schmölter & von Savigny, 2022). In addition, several other factors can also affect the ionospheric density and influence the delayed ionospheric response, such as geomagnetic activity, photochemical, dynamical, and electrodynamic processes (e.g., Ren et al., 2018; Schmölter et al., 2020; Vaishnav et al., 2018, 2022). Based on observational studies, Schmölter et al. (2020) reported that the delayed ionospheric response is influenced by geomagnetic activity. In addition, initial studies indicate that the delayed ionospheric response over Southern Hemisphere stations is greater than over Northern Hemisphere stations (e.g., Schmölter et al., 2020; Vaishnav, Schmölter, et al., 2021). Recently, Schmölter et al. (2022) discussed the height dependence of the delayed ionospheric response in detail and suggested the role of vertical transport.

To improve our understanding of the TI system, the Global-scale Observations of the Limb and Disk (GOLD) (Eastes et al., 2017) mission was launched in 2018. GOLD provides various parameters such as O_2 , O/N_2 , nighttime Nmax, and the solar proxy Q_{EUV} . The capabilities of GOLD have been discussed by several authors in recent publications (e.g., Oberheide et al., 2020). Schmölter et al. (2021) examined the delayed ionospheric response using the GOLD Q_{EUV} and the International GNSS Service (IGS) TEC. They highlighted the capability of GOLD for further investigation. In this paper, we focus on the study of ionospheric properties using these different parameters measured by GOLD and investigate their behavior during periods of low solar activity. Apart from solar forcing, lower atmospheric forcing and geomagnetic activity effects are relatively more pronounced during periods of low solar activity (Ma et al., 2012). Therefore, the availability of GOLD observations during the period of low solar activity allows us to investigate the relationship between TI parameters and solar indices under the influence of other forcings (e.g., lower atmospheric forcing and geomagnetic activity). Validating the various parameters against the solar proxies allows us to better understand rather quiet conditions, which then allows us to study the difference with disturbed conditions (larger storms or solar flares) during solar maximum, where we can compare the characteristics and evaluate the difference between the various external forcing sources in the TI system. Since the GOLD observations have previously been used to explain the delayed ionospheric response (Schmölter et al., 2021), we continue to investigate the solar-ionospheric relationship and confirm the GOLD capabilities for future study of the delayed response.

In the current analysis, we primarily investigate the behaviour of various parameters such as O_2 , O/N_2 , and nighttime Nmax observed by the GOLD mission as well as the relationship between Nmax and solar proxies at different time scales. We also take advantage of a global circulation model (GCM), namely the Coupled Thermosphere Ionosphere Plasmasphere electrodynamics (CTIPE) model (Fuller-Rowell & Rees, 1983). This model cannot be expected to accurately represent the actual variability of the TI system due to limited representation of the various processes and the precise inputs (Codrescu et al., 2012; Vaishnav, Schmölter, et al., 2021), however, it is useful to study TI processes that are implemented in it. In particular, the CTIPE model is capable of reproducing the delayed ionospheric response and investigating its physical mechanisms (e.g., Vaishnav, Jacobi, et al., 2021; Vaishnav, Schmölter, et al., 2021).

The CTIPE model has already demonstrated its capabilities in this regard (e.g., Codrescu et al., 2012; Vaishnav, Jacobi, et al., 2021; Vaishnav, Schmölter, et al., 2021). Notwithstanding several limitation like low spatial and

temporal resolution, model experiments increase our understanding of processes. Therefore, we performed a comparison between parameters observed by GOLD and predicted by the CTIPE model. Also in this study, we investigate the ionospheric delay using model simulated TEC and observed TEC against solar proxies during a selected period from 16 November to 12 December 2020, motivated by the previous findings by Schmöller et al. (2021), and the availability of the GOLD observations.

The manuscript is arranged as follows. Section 2 gives an overview of the data sets used, such as solar proxies, GOLD measurements, the O/N_2 measured with the Global Ultraviolet Imager (GUVI) and observed TEC, and the CTIPE model used to simulate the TI parameters. In Section 3, we present the results of comparing GOLD measured Q_{EUV} , O/N_2 , O_2 density, and nighttime Nmax with the values simulated by the CTIPE model. In addition, we estimate the delayed ionospheric response and discuss its relation to the GOLD observed and model-simulated O/N_2 . Section 4 discusses the results and concludes the paper.

2. Observations and Model

We use various solar indices and TI observations. The F10.7 index (Tapping, 2013) is commonly used to represent solar activity. Here we use the daily F10.7 index values available through the LASP LISIRD database (LASP, 2022). We make use of the daily Kp indices from the OMNIWeb Plus database (NASA, 2022d) to describe geomagnetic activity. The Solar EUV Monitor (SEM, Judge et al., 1998) aboard the Solar Heliospheric Observatory (SOHO) has monitored solar EUV fluxes in the 26–34 nm and 0.1–50 nm wavebands since 1996. In this study, we used the central-order flux at 1 AU (0.1–50 nm) with hourly and daily resolution. The SOHO/SEM EUV fluxes (hereafter EUV) are available at http://www.usc.edu/dept/space_science/semdatafolder/long/. To show the spatial and temporal behavior of the ionosphere, 1- and 2-hourly global TEC maps from the international GNSS service (IGS, Hernández-Pajares et al., 2009) were used. The maps are available from NASA (NASA, 2022a) with a spatial resolution of $2.5^\circ/5^\circ$ in latitude and longitude.

The GOLD (Eastes et al., 2017) instrument is installed aboard the SES-14 communications satellite, which was launched on 25 January 2018, into a geostationary orbit at 47.5°W longitude. GOLD has two identical independent imaging spectrographs covering the wavelength range 134–162 nm, called Channel A and Channel B (Eastes et al., 2020). The physical quantities such as the daytime neutral temperatures, the daytime and nighttime O_2 profiles, the daytime exospheric neutral temperature on the limb, the daytime O/N_2 , and Q_{EUV} are retrieved from the observed spectra. GOLD's unique orbit and imaging capabilities enables near hemispheric measurements of dayside O/N_2 column density ratios. During the day, the GOLD imager observes Earth's airglow emissions from about 134 to 162 nm with a spectral resolution of 0.2 nm, while at night it observes O I 135.6 nm emissions (Correia et al., 2021). The O/N_2 retrieval algorithm was developed for use with Global Ultraviolet Imager (GUVI) and Special Sensor Ultraviolet Spectrographic Imager (SSUSI) radiance images (Strickland et al., 1995). This algorithm has been applied for GOLD retrievals, but takes advantage of transmitting the full spectrum to maximize the signal-to-noise ratio (NASA, 2022c). In this study, we used version 4 data. GOLD also provides the daytime Q_{EUV} . Q_{EUV} is a solar EUV proxy describing the integrated irradiance below 45 nm derived directly from far ultraviolet (FUV) irradiance measurements using a look-up table approach (Strickland et al., 1995). It depends on the observed O I 135.6 nm radiance, the solar zenith angle, and the O/N_2 (NASA, 2022c). The temporal sampling is about 5 s. A complete description of the GOLD Q_{EUV} algorithm can be found in Correia et al. (2021).

GOLD performs nighttime scans of the disk in both hemispheres from $\sim 20:00$ to $00:30$ UT, which are used to derive the peak electron density Nmax from the measured intensity at 135.6 nm using the following simple assumptions: neglect of ion-ion mutual neutralization and multiple scattering, the electron n_e and atomic oxygen ion O^+ densities are equal, $n_e = n_{O^+}$, and the n_e profile is a Chapman layer profile (NASA, 2022c). Further, GOLD stellar occultation measurements are used to derive the O_2 absolute density profile ($\text{molecules}/\text{cm}^3$) on the limb. Occultations occur at latitudes from 60°S to 45°N and at all local times during the day. The algorithm of the measurements is based on the Polar Ozone and Aerosol Measurement (POAM) solar occultation algorithms (Lumpe et al., 2002). As the star rises or sets relative to the satellite position the stellar spectrum is measured across the GOLD spectral bandpass, from ~ 134 to ~ 162 nm. A complete description of the GOLD O_2 algorithm can be found in Lumpe et al. (2020). GOLD data sets are available online at <http://gold.cs.ucf.edu/search/>.

In addition, we also used the GUVI O/N_2 observations. The GUVI instrument aboard the NASA TIMED satellite provides FUV spectra (wavelength range 115–181 nm) from the thermosphere that include five bands: $Ly - \alpha$ at 121.6 nm, OI at 130.4 and 135.6 nm, and two parts of the N_2 LBH band system, namely the short LBH band

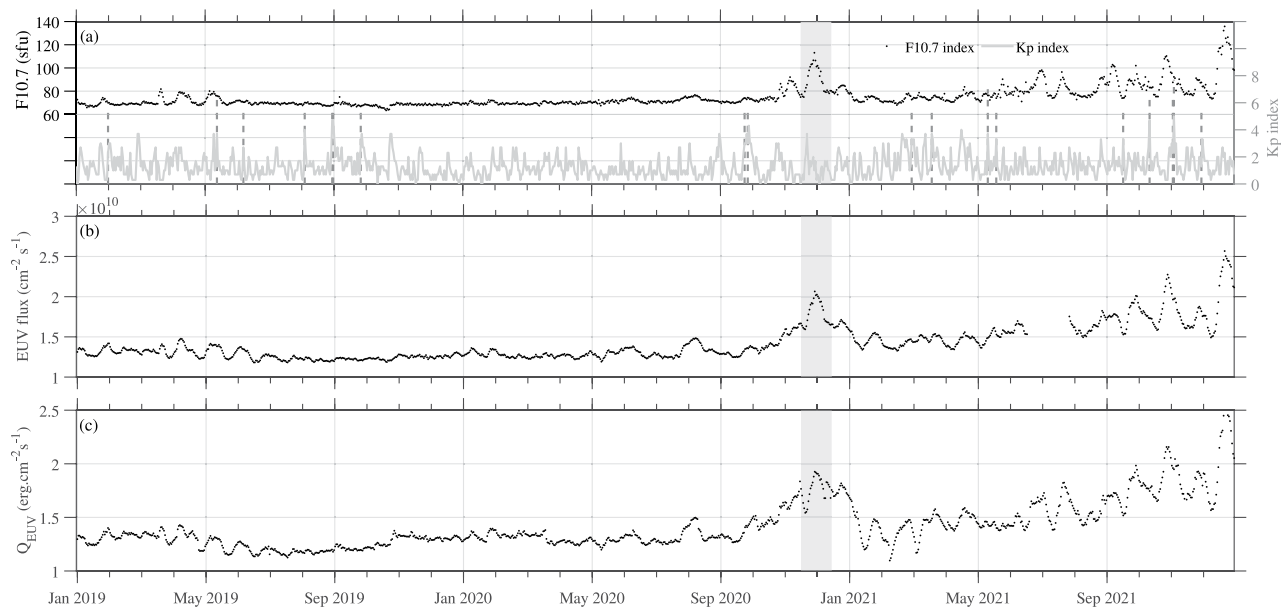


Figure 1. Solar proxies and geomagnetic indices during 2019–2021. The upper panel (a) shows the F10.7 index (dotted black) along with the daily Kp indices (gray curve) and $Kp > 5$ based on the 3 hourly Kp indices (vertical dashed gray lines). The middle panel (b) shows daily EUV fluxes provided by the SOHO/SEM satellite, while the lower panel (c) shows the GOLD daily average Q_{EUV} . The shaded region is the period used for the investigation of the delayed ionospheric response.

(LBHS) between 141 and 153 nm and the long wavelength LBH band between 167 and 181 nm on both the day and night sides (Christensen, 2003). The TIMED/GUVI dayglow data at O 135.6 nm and the N_2 LBHS were used to derive O/N_2 referenced at a fixed N_2 column density of $1 \times 10^{17} \text{ cm}^{-2}$. For our analysis, small-scale fluctuations were removed and data gaps were filled with running averages. GUVI O/N_2 data sets are available at: <http://guvitimed.jhuapl.edu/data/products>. The GUVI observations are used for validation purposes only and the main objective is to analyze GOLD observations.

The CTIpe model is a GCM from about 80 km to about 450 km altitude (Codrescu et al., 2008, 2012). Here we used the same model version as described in Vaishnav, Schmolter, et al. (2021) to study the TI parameters and simulate the neutral composition. In this version, F10.7 was used as the solar proxy. The EUV spectra in the CTIpe model used to calculate ionisation, dissociation, and heating in the TI are calculated from a reference spectra based on F10.7. The tidal forcing is applied at the lower boundary from the Whole Atmosphere Model (WAM). For comparison with nighttime N_{max} , O_2 , and O/N_2 ratios observed from the GOLD mission, we simulated the same period from 2019 to 2021. The simulated data were analyzed in the same manner as the observed data, which will be discussed in the Results section below.

3. Results

We aim to investigate the behavior of the TI system during the minimum of solar cycle (SC) 25. This section shows the results and discusses the GOLD observations (Q_{EUV} , O_2 , O/N_2 , and N_{max}) and their comparison with the modeled parameters during 2019–2021. We also analyze the relationships with the solar flux measurement and the delayed ionospheric response during the selected period from 16 November to 12 December 2020. To achieve the main objectives, a series of comparisons and cross-correlation analyses are performed, using both observations and model simulations. We will address the following points:

- The relationship between the solar proxies (F10.7, EUV, and Q_{EUV}).
- Variations in the GOLD observed parameters (N_{max} , O/N_2 and O_2 density profiles) and CTIpe simulated parameters.
- Cross-correlation analysis of ionospheric parameters (e.g., TEC and N_{max}) with solar proxies to investigate the ionospheric response at low solar activity.
- The delayed ionospheric response and modulation of O/N_2 during 16 November to 12 December 2020, which is shown in the shaded region of Figure 1 below.

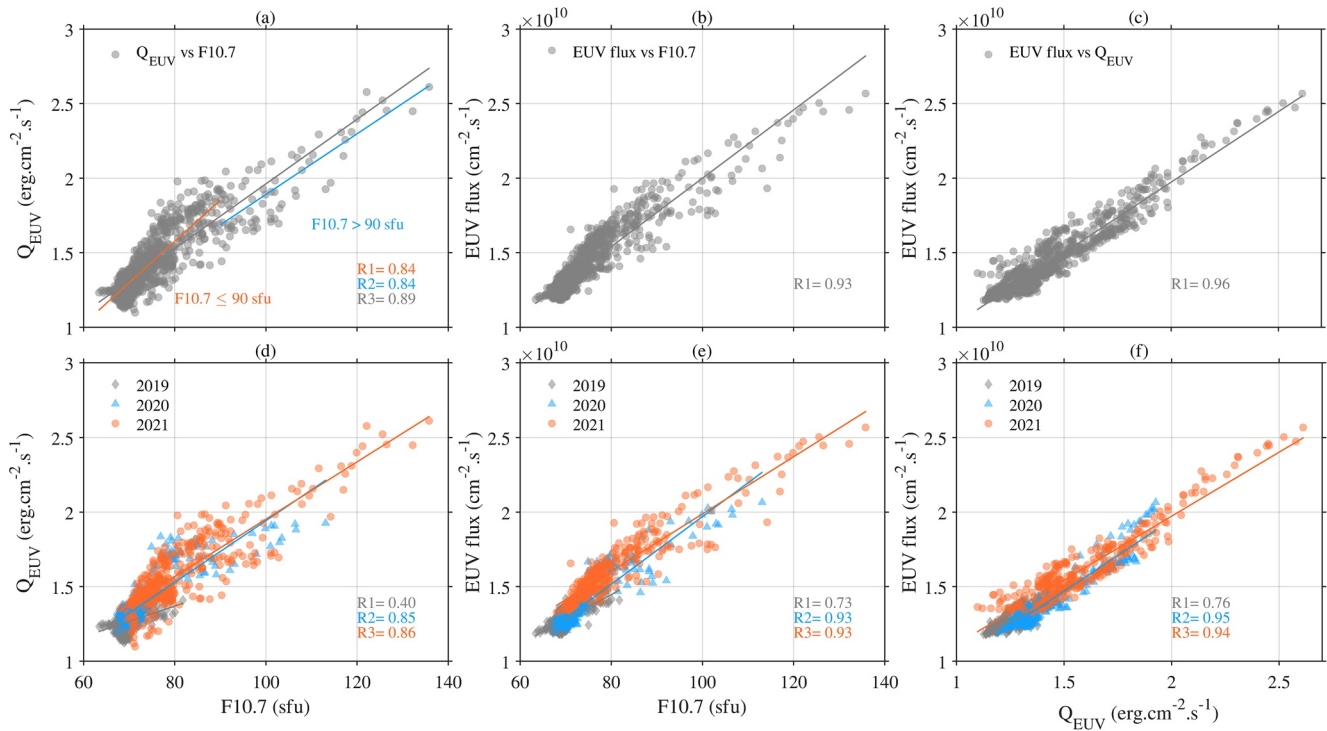


Figure 2. Top panel: Cross-correlations between the (a) daily Q_{EUV} and F10.7 (gray) along with the cross-correlation for F10.7 > 90 sfu (blue) and for F10.7 \leq 90 sfu (red), (b) EUV and F10.7, and (c) Q_{EUV} and EUV in 2019–2021. Bottom panel: Cross-correlations between the (d) daily Q_{EUV} and F10.7, (e) EUV and F10.7, and (f) Q_{EUV} and EUV during 2019 (gray), 2020 (blue), and 2021 (red). The cross-correlations R and the fitting lines are marked with the corresponding colors in the panels.

3.1. Solar Flux Variability

The full solar spectrum cannot be measured from the ground, since the solar EUV radiation, among others, is absorbed in the upper atmosphere. Direct measurement of EUV radiation is possible from space, but the problem of on orbit solar instrument degradation is a challenge (e.g., BenMoussa et al., 2015). However, there are several solar proxies that are available over long periods of time. Of the available proxies, the F10.7 index is the most commonly used for the EUV band (Dudok de Wit et al., 2009). Therefore, in this work, we consider both the F10.7 index and EUV to compare with the Q_{EUV} .

Figure 1a shows the time series of the F10.7 index together with the Kp index during years of low solar activity from 2019 to 2021, with an average F10.7 of less than 80 sfu. Some clear 27-day solar rotation cycles are observed in 2019 and 2020, therefore these periods can be used to study the delayed ionospheric response to solar activity. The F10.7 index is low in 2019 and has increased slightly since November 2020, indicating the recovery of solar activity from solar minimum and the beginning of the ascending phase of SC 25. The shaded region shows the period from 16 November to 12 December 2020, which was used to study the ionospheric response to solar EUV variations. The daily Kp index indicates generally weak geomagnetic activity during the study period. The few vertical dashed gray lines indicate $Kp > 5$, based on the 3 hourly Kp indices, which indicates stronger variations in geomagnetic indices on the short time scale.

Figures 1b and 1c show the variations of the EUV and Q_{EUV} observations, respectively. The overall response is quite similar and the variations are more pronounced than for the F10.7 index. In general, the F10.7 index hardly changes from June 2019 to October 2020, as shown in Figure 1a, but the EUV and Q_{EUV} nevertheless show fluctuations during this period. The variations of Q_{EUV} are comparable to the ones of EUV, which is explained by the fact that Q_{EUV} also covers the same wavelength band measured with SOHO/SEM. Generally, all solar proxies are strongly correlated. To estimate the correlation, here we use the Pearson correlation coefficient.

Figure 2 shows the correlation analysis between the F10.7 index, EUV, and Q_{EUV} . Figure 2a shows that the correlation coefficient between Q_{EUV} and the F10.7 index is about 0.89. A stronger correlation of about 0.93 is seen between EUV and the F10.7 index (Figure 2b). A similar correlation coefficient of about 0.96 is observed

between Q_{EUV} and the EUV (Figure 2c). The overall correlation during 2019–2021 is higher between Q_{EUV} and EUV flux as compared to F10.7 and Q_{EUV} . Similar results were reported by Schmölter et al. (2021) by using the correlation analysis for 2019. They also found that the correlation increases at longer time scales. The cross correlation is calculated for two categories of F10.7 > 90 sfu (blue) and F10.7 ≤ 90 sfu (red). For both conditions, the cross correlation is about 0.84. Figure 2 also shows the resulting linear fits between the solar proxies.

The bottom panel of Figure 2 shows the cross-correlation between (d) daily Q_{EUV} and F10.7 indices, (e) EUV and the F10.7 index, and (f) Q_{EUV} and EUV for each year from 2019 to 2021. The overall correlation is lower in 2019. The maximum correlation in 2019 (2020) is about 0.76 (0.95) between Q_{EUV} and EUV, while the correlation between Q_{EUV} and F10.7 is lower at about 0.40 (0.85). In 2021, the overall correlation is stronger than in 2019, and similar to 2020. The overall correlation increases with solar activity and all solar indices correlate well with each other in 2020 and less strongly in 2019. Furthermore, we also analyzed the solar proxies from 16 November to 12 December 2020 (as shown in the shaded region of Figure 1). Our analysis showed a stronger correlation between EUV and F10.7 of about 0.93, compared to the correlation with Q_{EUV} , about 0.81 (Figure not shown).

Understanding the variations in solar activity is important for studying the response of ionospheric parameters such as Nmax or TEC, which are strongly influenced by solar activity. The GOLD mission provides nighttime Nmax observations, which, however, depend on the previous daytime values, so that correlation between solar proxies and nighttime Nmax is expected. Previous studies have demonstrated that Nmax during nighttime is linearly correlated with solar proxies during periods of low and moderate solar activity (Richards, 2001). In the next section, we will first examine the GOLD Nmax characteristics in detail and compare them with the model simulated Nmax. In addition, we will examine the relationship between the nighttime Nmax and solar activity.

3.2. Comparison Between GOLD and Modeled Nmax

In this section, we investigate the response of nighttime Nmax to solar activity. Here we first examine seasonal variations using the mean Nmax observations from GOLD during March equinox and June solstice from 2019 to 2021. Figure 3 shows the GOLD Nmax distributions at the March equinox (top panel) and June solstice (bottom panel) in 2019, 2020, and 2021. Nmax values are larger during the March equinox than at the June solstice. In addition, Nmax is higher in 2021 than in 2019 and 2020 due to the increase in solar activity within SC 25. Compared to the June solstice, there is a more prominent increase in Nmax around the equator (equatorial ionization anomaly, EIA; Appleton (1946)) during the March equinox. The electron density is more evenly distributed at low- and mid-latitudes during the June solstice.

Figure 4 shows the zonal mean daily Nmax from 2019 to 2021 as observed by GOLD and simulated by CTIPE. Latitudes were selected according to the availability of GOLD observations. In GOLD Nmax, a clear EIA structure can be seen with higher Nmax on both sides of the magnetic equator during March equinox compared to June solstice (Figure 4a). Nmax values increase with solar activity. Compared to GOLD Nmax, the modeled Nmax values are more pronounced but show similar latitudinal and seasonal variations (Figure 4b). The seasonal variations are due to the semiannual fluctuations of Nmax (Qian et al., 2013). In addition, Nmax is higher in March (July) in the Northern (Southern) Hemisphere. In July–August, EIA crest differences between hemispheres were observed, possibly due to summer-to-winter neutral wind effects (Lin et al., 2007). A larger discrepancy between model and observations is evident. In October–November 2021, the observed Nmax is larger than during the rest of the study period. This is due to higher solar activity leading to more ionisation and contributing to Nmax, while the model cannot reproduce such strong variations.

To investigate the solar-ionospheric relationship, we first examine the correlation between unfiltered data-sets, namely observed/modeled Nmax and solar measurements (Q_{EUV} , EUV, and F10.7) from 2019 to 2021 at 0° geographic latitude. Correlation coefficients for GOLD Nmax (CTIPE Nmax) with EUV, Q_{EUV} , and F10.7 are 0.55(0.30), 0.44(0.24), and 0.41(0.21), respectively. The overall correlation is low; however, the correlation for solar indices with GOLD Nmax is higher than with the CTIPE Nmax. Schmölter et al. (2020) suggested that geomagnetic activity could also affect the ionospheric densities. Therefore, we investigate the possible role of geomagnetic activity by calculating the correlation coefficient between Nmax and the Kp index from 2019 to 2021 at 0° geographic latitude. The correlation coefficient for GOLD/CTIPE Nmax with the Kp index is about 0.33/0.24. During periods of low and moderate solar activity, other dominant factors such as lower atmospheric forcings (e.g., tides, gravity waves, and planetary waves) and geomagnetic activity can influence the ionospheric

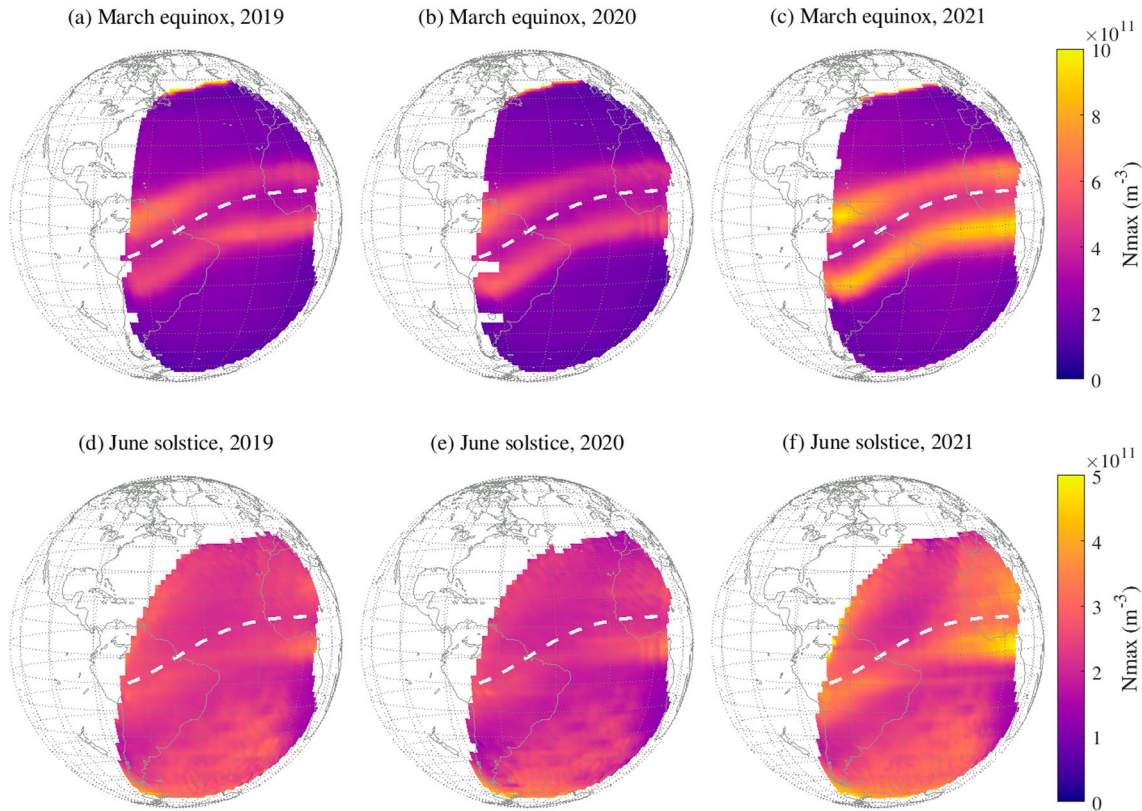


Figure 3. The GOLD nighttime N_{max} variations at March equinox (upper panel) and June solstice (lower panel) during 2019, 2020, and 2021. The season and year are indicated in the respective panel title. Note the different scaling of the two rows. The white dashed line represents the magnetic equator.

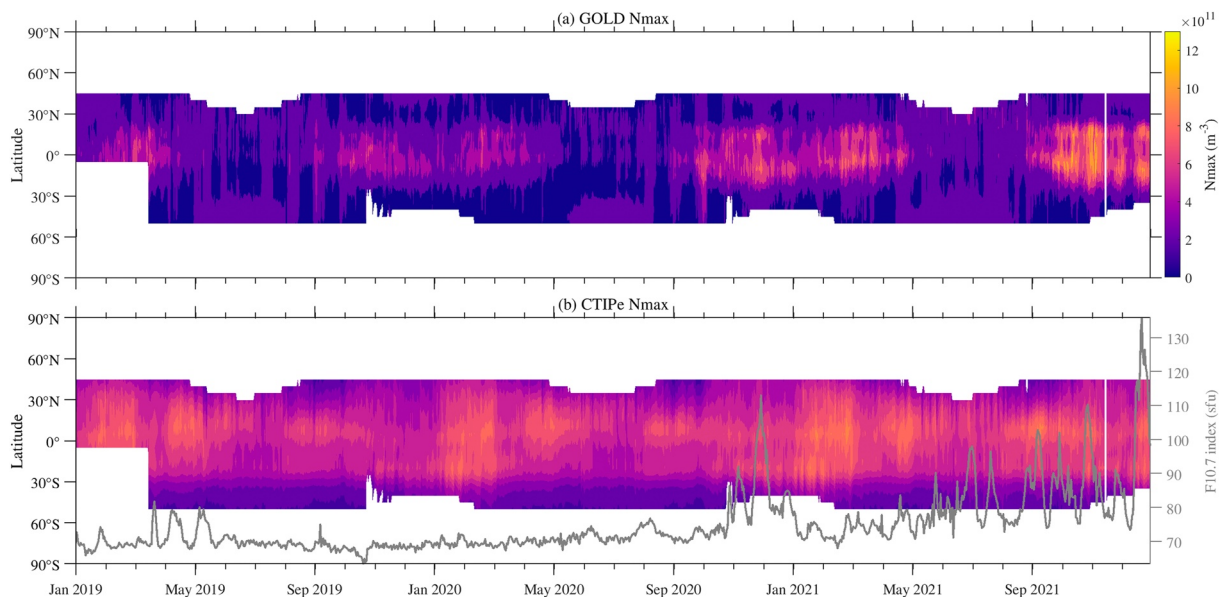


Figure 4. The variations and comparison of daily zonal mean nighttime N_{max} (a) observed from GOLD and (b) simulated by CTIPe model during January 2019 to December 2021. The zonal mean N_{max} is calculated over the longitude range (128° W to 35° E) available from GOLD. In the lower panel, the right y-axis shows F10.7 (gray curve).

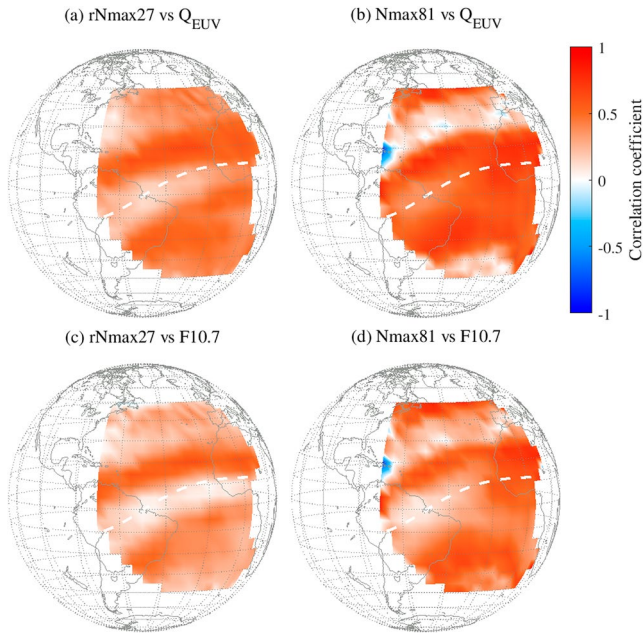


Figure 5. Cross-correlation maps for (a, c) GOLD rNmax27 (27-day variations), and (b, d) GOLD Nmax81 (after removing variations less than 81 days) against Q_{EUV} (top panel) and F10.7 (bottom panel) calculated over the period 2019 to 2021. The white dashed line represents the magnetic equator.

parameters more strongly (Fang et al., 2013; Gan et al., 2020; Tsurutani et al., 2009). These factors could be the reason for the poor correlation between solar indices and ionospheric parameters (Vaishnav et al., 2019).

The GOLD Nmax data sets are characterized by annual, semiannual and 27-day variations. Therefore, we further investigate the correlation between GOLD Nmax, Q_{EUV} and F10.7 during the medium (27-day variations) and long-term ionospheric response (81-day averages). The medium term ionospheric response to the 27-day solar variability has been discussed by several authors (e.g., Kutiev et al., 2013; Vaishnav et al., 2019). These variations in the ionosphere are caused by the 27-day variations in solar irradiance and geomagnetic activity (Ma et al., 2012). To focus only on the 27-day variations, we first performed a smoothing procedure following Ma et al. (2012). In this method, a 33-day moving average was applied and shifted 1 day forward in time on the time series of Q_{EUV} , EUV, and Nmax. The relative changes can be determined by Equation 1:

$$\Delta A_i = (A_i - \mu) / \mu, \quad (1)$$

where A_i represent the time series of Q_{EUV} , EUV and Nmax, while μ represents the 33 days moving averages of A_i . To focus only on the 27-day variations, we then applied zero-phase Butterworth bandpass filter between 22 and 33 days to the time series of $\Delta Nmax$, ΔQ_{EUV} and ΔEUV from Equation 1, which we refer to below as the filtered time series (rNmax27, after bandpass filtering). The correlation maps for rNmax27 with filtered Q_{EUV} and F10.7, using observations from 2019 to 2021, are shown in Figures 5a and 5c. The maximum correlation between rNmax27 and Q_{EUV} is approximately 0.7 in the

mid latitude region. Conversely, the correlation coefficients are relatively low (about 0.3) in the equatorial region, which can be attributed to atmospheric dynamics process causing vertical plasma motion (Lee et al., 2012). Poleward of about 30°N, the correlation coefficients decrease toward mid latitudes. The correlation is generally higher in the Northern Hemisphere. The correlation between rNmax27 and F10.7 is lower than that of Q_{EUV} , with a maximum of around 0.5 in the mid-latitude region, as shown in Figure 5c. We also investigate the correlation between rNmax27 and the Kp index, since the geomagnetic activity associated with the solar wind, which also has a periodicity of 13.5 and 27 days (Altadill & Apostolov, 2003). We found the correlation coefficient of about 0.6 between rNmax27 and Kp indices at 0° latitude.

In addition, 81-day running averages are used to estimate the long-term variations of Nmax (Nmax81). The correlation maps for Nmax81 with the filtered Q_{EUV} and F10.7 indices are shown in Figures 5b and 5d. The correlation coefficient for Nmax81 with Q_{EUV} is about 0.8 in the mid-latitude region. Similarly, F10.7 shows a higher correlation with Nmax81 at mid-latitudes. However, Nmax is less strongly correlated to F10.7 at low latitudes compared to Q_{EUV} .

Our analysis of the ionosphere's response to solar and geomagnetic activity shows that long-term responses (averaging 81 days) have stronger correlation coefficients than medium-term ones (27-day solar variations). Compared to F10.7, GOLD Q_{EUV} correlates more strongly at long-term responses. We also found that Nmax correlates well with geomagnetic activity for medium-term ionospheric responses. Notably, despite the low solar activity, there is a stronger correlation of about 0.8 between the GOLD Nmax and solar indices for the long-term response. It would be interesting to gain new insights by analyzing the relationship between these parameters during periods of high solar activity using GOLD observations.

3.3. Comparison Between GOLD, GUVI, and Modeled O/N_2

In addition to solar irradiance, the thermospheric O/N_2 is a key parameter in determining the composition changes in the TI system. This parameter is very well studied and very important when it comes to the delayed ionospheric response. The daytime ionospheric F2 electron density highly depends on the O , N_2 , and O_2 densities, which are photoionized by EUV, for the production (q) of ions and electrons (e.g., $O + h\nu \rightarrow O^+ + e^-$). These electrons and

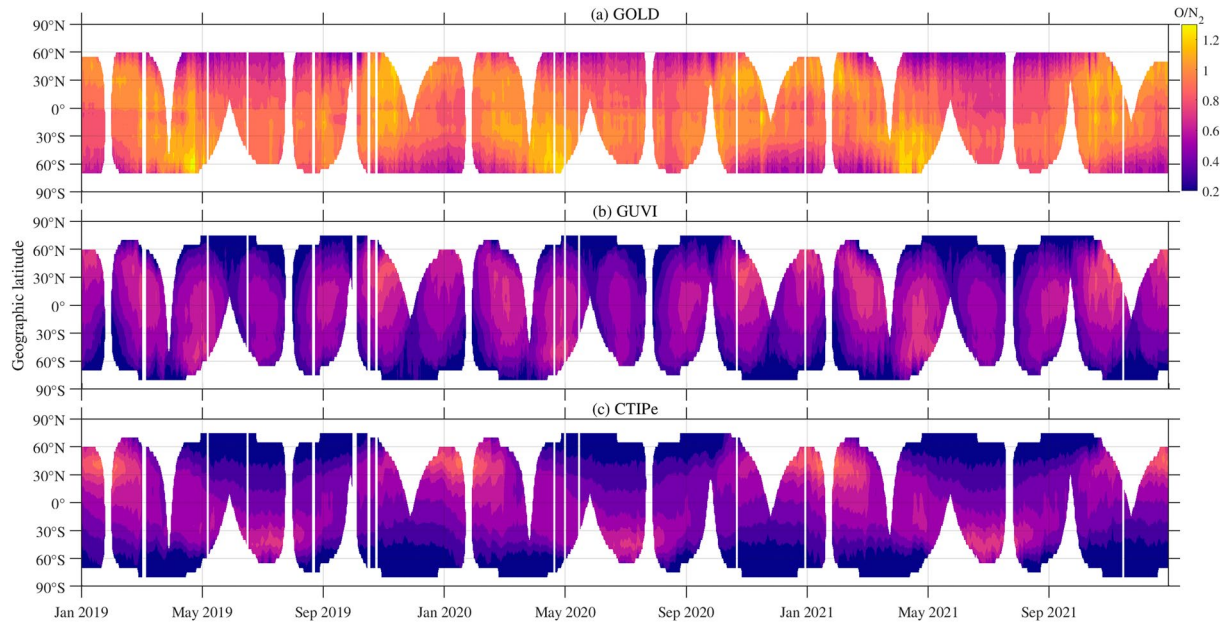


Figure 6. Variations in the daily O/N_2 ratio observed from (a) GOLD, (b) GUVI, and those simulated by the (c) CTIPe model from January 2019 to December 2021.

ions are lost (β) by recombination through several possible processes (e.g., $O^+ + N_2 \rightarrow NO^+ + N$ followed by $NO^+ + e \rightarrow N + O$ and $O^+ + O_2 \rightarrow O_2^+ + O$ followed by $O_2^+ + e \rightarrow O + O$) (Rishbeth, 1998). The production of O^+ depends on both O density and solar radiation flux I .

The steady-state electron density N for the F2 region is given by Rishbeth (1998):

$$N \sim \frac{q}{\beta} \sim \frac{I[O]}{\gamma_1[N_2] + \gamma_2[O_2]} \quad (2)$$

where γ_1 and γ_2 are the reaction rate coefficients. The production term q depends mainly on the atomic oxygen concentration and the loss term β mainly on N_2 with small contribution from O_2 , since N_2 is more abundant than O_2 by a factor of 10–20. Hence, q/β mainly depends on the O/N_2 ratio.

GUVI, GOLD, and the modeled O/N_2 were calculated according to the concept introduced by Strickland et al. (1995). Because of the high resolution of the GOLD wavelength spectra, it is possible to isolate specific wavelength bands from the LBH band system. However, in previous missions (e.g., GUVI) this possibility was limited because typically as much of the LBH band system as possible was included in the measured passband to maximize the overall signal. To calculate O/N_2 , Strickland et al. (1995) suggested that the O/N_2 column density ratio is proportional to the 135.6 nm/LBH intensity ratio, referenced to an N_2 depth of 10^{17} cm^{-2} . The O/N_2 ratio observed by GUVI and the one simulated by the model are calculated using the same method. Correira et al. (2021) indicate possible biases of 10% in GOLD O/N_2 due to the EIA.

Here we compare the modeled O/N_2 ratio to the observed ones. For this the daily mean O/N_2 observed from GOLD, GUVI and simulated by the CTIPe model have been used. The model simulated O/N_2 was calculated at the intersection of the fields of view of GOLD and GUVI. Figure 6 shows the variations in O/N_2 observed by (a) GOLD and (b) GUVI, and those simulated by (c) the CTIPe model. The O/N_2 simulated by the model underestimates the observations in as shown in Figure 6. There are significant differences between the simulated and the observed O/N_2 . The GUVI O/N_2 ratio is lower compared to the GOLD O/N_2 and higher than CTIPe O/N_2 . Also at low and mid latitudes, more O/N_2 variability is found in the GOLD observations compared to the CTIPe O/N_2 . Qian et al. (2022) also compared the GOLD O/N_2 with the NRLMSISE-00 predictions and GUVI observations. They also reported a higher GOLD O/N_2 compared to the other two. They found a hemispheric asymmetry in the seasonal variations of the O/N_2 and annual and semiannual patterns are observed in the Southern Hemisphere, whereas an annual variation dominates in the Northern Hemisphere. Similar annual and seasonal variations were also found in CTIPe O/N_2 . The seasonal dependency of O/N_2 variability can be related to the seasonal variation

Table 1
Count of GOLD O_2 Density Profiles Available at Three Locations in 2019 and 2020

Year	Latitude/Longitude		
	2°N, 33°E	21°N, 32°E	28°S, 33°E
2019	82	96	67
2020	85	85	66

of geomagnetic activity and mean circulation (Martinez & Lu, 2023). They investigated the day-to-day variations in the GOLD O/N_2 and its correlation with the geomagnetic activity (Dst index). They found that the correlation increases in summer/spring and O/N_2 increases during autumn, while the correlation decrease in winter and autumn whereas O/N_2 decreases toward summer.

Furthermore, it is known from previous studies that the delayed ionospheric response is mainly related to the change in the O/N_2 ratio due to transport process (Vaishnav, Schmöler, et al., 2021). Considering this fact, we further investigate the delayed ionospheric response and examine the response of the

O/N_2 ratio during the study period in Section 3.6. As mentioned earlier, the electron density of the ionospheric F2 layer depends on the densities of O , N_2 , and O_2 during daytime. Therefore, in the next section, we discuss and compare the O_2 density profiles observed by GOLD and simulated by the model to take advantage of the capabilities of GOLD.

3.4. Comparison Between GOLD and Modeled O_2 Density

GOLD provides O_2 density profiles from 100 to 250 km, which we compare with simulated O_2 by CTIPe. Since GOLD O_2 data is limited and not always available, we only utilized data from three locations at 2°N, 33°E; 21°N, 32°E, and 28°S, 33°E during 2019 and 2020. The total number of profiles for the above locations is less than 100 (Table 1) and they are available at different times. Therefore, we sorted the simulated O_2 profiles for the same time and day as the profiles observed by GOLD and plotted a mean with standard deviation (shaded regions) in Figure 7. The top panel shows the O_2 density profiles for 2019 and the bottom panel shows the ones for 2020.

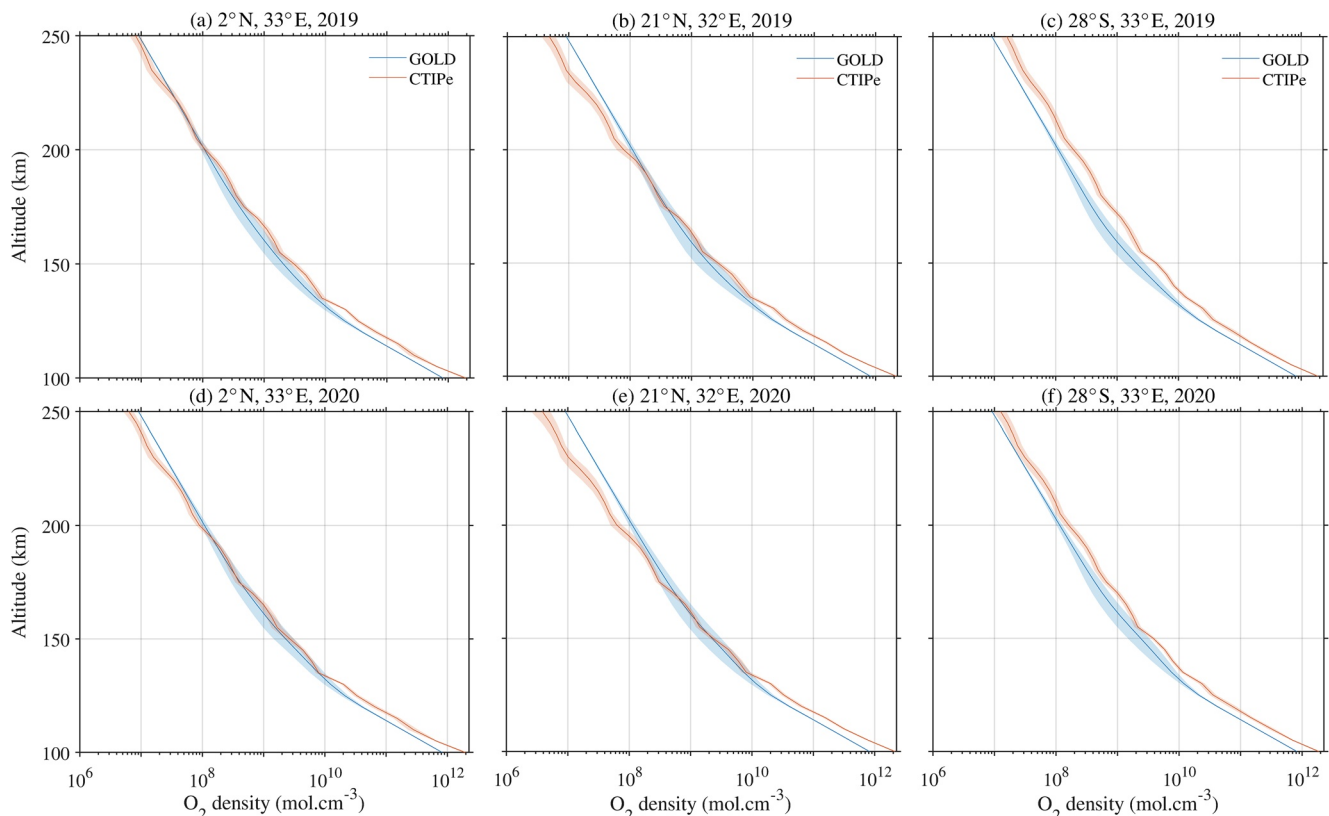


Figure 7. Comparison between the mean O_2 density along with its standard deviation (shaded regions) observed by GOLD and CTIPe model simulated for 2019 (upper panel) and 2020 (lower panel) at (a, d) 2°N, 33°E, (b, e) 21°N, 32°E, and (c, f) 28°S, 33°E.

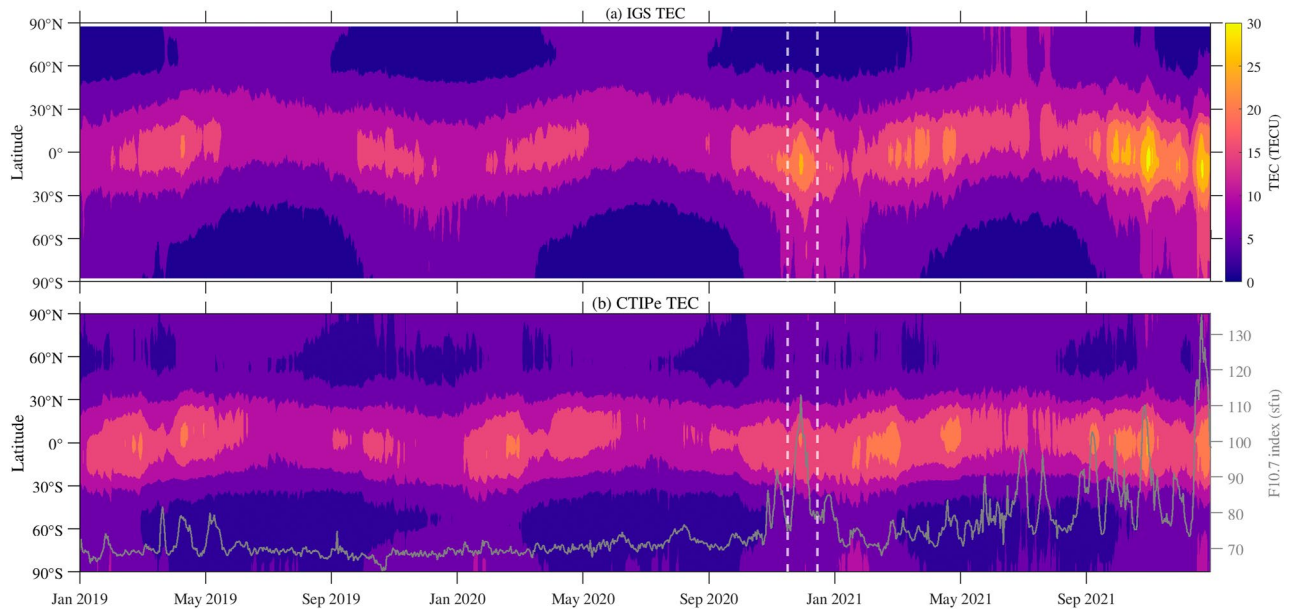


Figure 8. Temporal variations of the zonal mean observed TEC (a) and modeled TEC (b) from 2019 to 2021. The area between the dashed white lines shows the period from 16 November to 12 December 2020 used for the delayed ionospheric response study. In the lower panel, the right y-axis shows F10.7 (gray curve).

Lumpe et al. (2020) showed that the GOLD O_2 profiles have an estimated accuracy of 10% or less in the altitude range of 130–200 km. They suggested that this altitude range should be used for further scientific investigations. Figure 7 reveals that below 200 km, the CTIPe overestimates the GOLD O_2 at all selected locations during 2019. However, the O_2 density at 2°N, 33°E shows a good agreement between the model and observations (Figure 7a). On the other hand, the largest discrepancy between model and observation is seen in the Southern Hemisphere (28°S, 33°E, Figures 7c and 7f). In 2020, the difference between GOLD and CTIPe O_2 levels is significantly reduced between 130 and 170 km, as shown in Figures 7d–7f. Furthermore, the mean percentage difference ($\delta O_2 = [O_2^{obs} - O_2^{model} / O_2^{model}] \times 100\%$) between observed and simulated O_2 between 130 and 200 km at 2°N, 33°E; 21°N, 32°E, and 28°S, 33°E is about 24%, 12%, and 49% in 2019, while it is about 9%, 9%, and 37% in 2020.

Overall, the performance of the model is good in the Northern Hemisphere, while it has a larger bias in the Southern Hemisphere. Further, the observed O_2 density is generally lower than the simulated O_2 in earlier comparisons (Lumpe et al., 2020), which is also true for the CTIPe model. Furthermore, due to data limitations, the current analysis does not provide new insights into the influence of O_2 density on the delayed ionospheric response. But agreement with the model simulated O_2 density supports other results (Lumpe et al., 2020).

In summary, we have discussed the observed parameters from GOLD and compared them with the model simulations. In the next section, we mainly focus on the observed and simulated TEC and their relationship with the solar proxies.

3.5. Relation Between TEC and Solar Proxies

Figure 8 shows daily zonal mean TEC values for a fixed local time (12:00) from (a) IGS TEC maps and (b) CTIPe simulated values from 2019 to 2021. The maximum TEC of about 30 TECU can be observed in 2021, where the F10.7 index increases to about 120 sfu. Both observed and modeled TEC show strong semi-annual variations. However, the modeled TEC values are underestimated compared to the observed values. Codrescu et al. (2008) pointed out model limitations that lead to differences with observations, such as an artificial boundary between the low- and mid-latitude ionospheric model and the high-latitude ionospheric model, and a missing prompt penetration electric field.

To understand the relationship between the ionosphere and solar activity, we also consider the cross-correlation analysis between the daily TEC at fixed local time (12:00) provided by observations and model simulations, with F10.7 and daily mean Q_{EUV} . Global maps of correlations for 2019 to 2021 are shown in Figure 9. The spatial

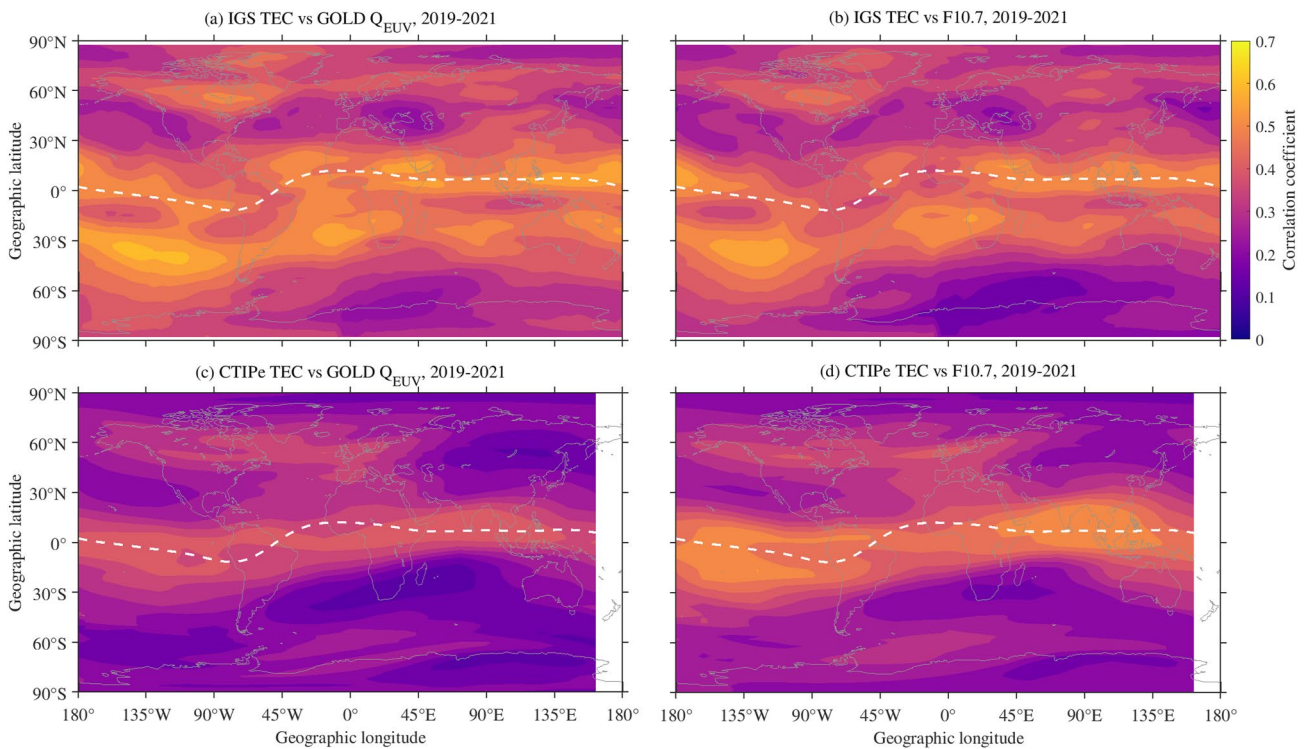


Figure 9. Correlation coefficients between TEC and F10.7 (Q_{EUV}), as a function of latitude and longitude using observed TEC (top), and modeled TEC (bottom) during 2019–2021. The time period and solar proxies used are indicated in the respective panel title. The white dashed lines represent the magnetic equator.

distribution of the calculated correlation coefficients is similar for both solar Q_{EUV} and F10.7. The upper (lower) panel shows the correlation maps for observed (modeled) TEC against F10.7 and Q_{EUV} . Figures 9a and 9b shows a stronger correlation of about 0.6 in the low and mid-latitude region, indicating that this region is more strongly affected by solar activity (Lee et al., 2012). A lower correlation of about 0.4 is seen in the high-latitude region and indicates that this region is strongly influenced by other factors, such as particle precipitation. The correlation between TEC and F10.7 (Figure 9b) appears to be lower than that between TEC and Q_{EUV} (Figure 9a), but the correlation is stronger than between CTIPe TEC and Q_{EUV} (Figure 9d). A higher correlation is expected since F10.7 is used as a proxy for solar wavelengths, which drives the model (Woods & Rottman, 2002). The lower correlation between the modeled TEC and Q_{EUV} (Figure 9c) suggests that the F10.7 index for solar flux could also be a factor that leads to inadequate modeling of TEC.

The current analysis confirms that the input parameters of the model are strongly correlated with the output parameters. Therefore, further studies are needed to analyze electron density measurements that are independent of the underlying models and thus of F10.7 (e.g., ionosondes). Recently, Vaishnav, Schmölter, et al. (2021) conducted a comparative study of solar irradiance using observed irradiance and irradiance calculated from empirical models and found significant differences. Therefore, implementation of an improved solar EUV spectrum in the model needs to be considered.

3.6. Delayed Ionospheric Response

Several authors have reported the delayed ionospheric response of about 18 hr to 2 days in ionospheric parameters, especially TEC and NmF2, depending on the resolution and solar EUV observations or proxies used (e.g., Jakowski et al., 1991; Jacobi et al., 2016; Ren et al., 2019; Schmölter et al., 2018, 2020, 2021; Vaishnav et al., 2019, & references therein). The delayed ionospheric response is calculated by cross-correlating hourly TEC values and EUV during the study period from 16 November to 12 December 2020 (shaded region shown in Figure 1). Figure 10 shows latitudinal variations of cross-correlations and ionospheric delay calculated at 80°W longitude and a fixed local time (12:00) using observed and modeled TEC and EUV. The longitude was chosen based on the maximum possible latitude range available for GOLD O/N_2 observations. The figure shows that the correlation is higher in the Northern Hemisphere than in the Southern Hemisphere. The ionospheric delay

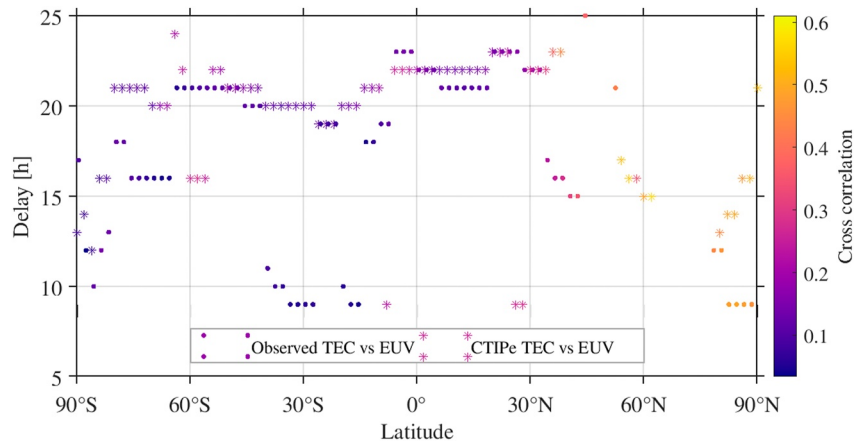


Figure 10. Latitudinal variations of the delayed ionospheric response and cross-correlations for observed (dots) and modeled (asterisks) TEC with the EUV flux during 16 November–12 December 2020 at 80°W longitude.

calculated between the EUV flux and the observed (modeled) TEC is marked with dots (asterisks), respectively. As described in the previous section, electron density varies with solar activity. Variations in solar activity cause compositional changes, which in turn affect the time delay.

In the previous section, we calculated correlation maps for daily resolution data sets of TEC and EUV. The results showed correlation coefficients of approximately 0.5–0.7 for daily data at low- and mid-latitudes (Figure 9). Conversely, hourly data sets exhibited weaker correlation coefficients ranging from 0.2 to 0.4 at low and mid-latitudes (Figure 10). The weaker correlation can be attributed to the presence of small-scale variabilities. We also noted that solar proxies (Q_{EUV} and F10.7) exhibit stronger correlations at longer timescales than at shorter or medium-time scales, as discussed in Section 3.2. The mean ionospheric delay calculated between the observed TEC and EUV is ≈ 15 hr with a standard deviation of ≈ 5 hr. In contrast, for the modeled TEC, the mean ionospheric delay is ≈ 16 hr with a standard deviation of ≈ 5 hr. The maximum ionospheric delay for the modeled TEC is about 24 hr, while it is about 23 hr for the observed TEC. The results show the latitudinal variations of the ionospheric delay which are caused by the compositional and thermospheric circulation changes. The model is capable of reproducing a similar delay to observations even during the period of low solar activity. Previously, Vaishnav, Schmölter, et al. (2021) had discussed the model's capabilities to reproduce the delay during periods of high solar activity. The study found an average delay of about 17 and 16 hr for observed and modeled TEC against solar EUV flux, respectively.

It is well established that O/N_2 modulates the delayed ionospheric response (Ren et al., 2018). The importance of photo-chemistry of O and N_2 and the steady state Equation 2 are shown in Section 3.3. To elucidate a probable source for the observed delayed ionospheric response, the O/N_2 ratio from GOLD, and simulated using CTIPe have been used for the time interval 16 November to 12 December 2020.

Figure 11 demonstrates the O/N_2 ratio from GOLD and CTIPe during the 27-day period analyzed in Figure 10 along with the EUV and Kp index. During this period, the GOLD O/N_2 ratio is larger in the Northern Hemisphere (Figure 11b). Similar variations can be seen in modeled O/N_2 (Figure 11d). Figure 11b show that the GOLD O/N_2 at mid latitudes in the Northern Hemisphere varies with EUV, suggesting a dependence on solar activity (e.g., Schmölter et al., 2021; Zhang & Paxton, 2011). In addition to solar activity, the O/N_2 ratio can also be influenced by lower atmospheric forcing and geomagnetic activity (Qian et al., 2009). The average geomagnetic activity was weak (mean Kp = 1.16). However, during the rising part of the solar activity, geomagnetic activity was somewhat stronger (daily Kp ≥ 3 , 3-hourly Kp up to 4.7), so the O/N_2 is larger. The solar activity peaks on the 13th day (29 November) and then continuously decreases until the 23rd day (08 December). The GOLD O/N_2 ratio is positively correlation with EUV in the Northern Hemisphere from 25°N to 55°N (Figure 11c). However, there is a negative correlation at other latitudes which may be influenced by geomagnetic activity and lower atmospheric forcing. To confirm this, we have also calculated correlation between O/N_2 and Kp index and found positive correlation in low- and mid-latitudes in the Northern Hemisphere (see Figure 11c). Although not all observed variations are reproduced by the model, it does show a positive correlation between CTIPe O/N_2 and EUV in mid-latitudes and Kp index positively correlates with the CTIPe O/N_2 in low- and mid-latitudes (Figure 11e). A

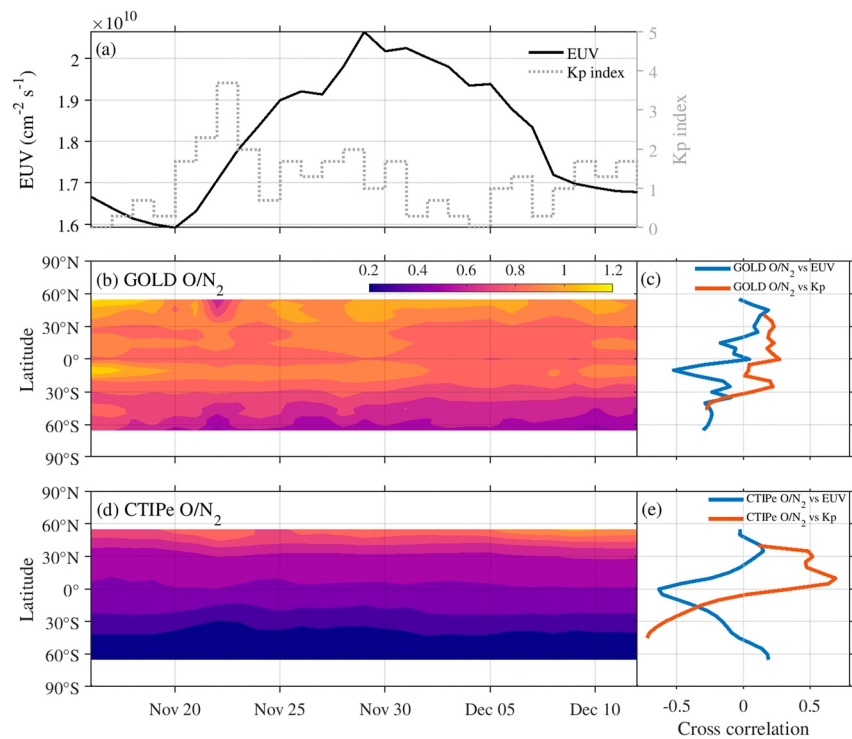


Figure 11. The upper panel (a) shows the EUV flux (solid black) along with the daily Kp indices (dotted gray curve). Variations of the O/N_2 during 16 November to 12 December 2020 from (b) GOLD and (d) CTIPe with the corresponding panels showing correlation with EUV and Kp index (c, d), as a function of latitude and days.

recent study by Schmölter et al. (2021) also investigates the influence of O/N_2 ratio on the delayed ionospheric response at 0° latitude-longitude during a low solar activity period and found no correlation between O/N_2 and solar proxies.

Our analysis indicates that the GOLD O/N_2 ratio positively correlates with EUV, suggesting that O/N_2 can affect the delayed ionospheric response in the Northern Hemisphere (25°N – 55°N). Whereas, a negative correlation at other latitudes indicates the possible role of other factors, like geomagnetic activity and lower atmospheric forcing, which affect the O/N_2 ratio, particularly during low solar activity (Luan et al., 2017; Qian et al., 2009).

4. Discussion and Conclusions

In the above analysis, we presented an overview of GOLD Q_{EUV} , O/N_2 , molecular oxygen density, and nighttime peak electron density N_{max} in the TI region during the minimum of SC 25, 2019 to 2021. The GOLD observations are compared with the CTIPe model simulated parameters to investigate the model capabilities. We analyzed three different solar proxies, namely SOHO/SEM EUV, F10.7, and Q_{EUV} , to investigate their correlation during low solar activity years. We found that Q_{EUV} strongly correlates with F10.7 and EUV with a coefficient of approximately 0.89 and 0.96, respectively. The correlation increases with solar activity. However, since the solar activity was low during 2019 and 2020 and only moderate in 2021, we still need more data from times of high solar activity to confirm our findings for solar maximum.

Next, we analyzed the seasonal variations of the GOLD nighttime N_{max} . Our results showed a larger increase in N_{max} around the equator during the March equinox compared to the June solstice. Additionally, the electron density was more evenly spread out during the June solstice at low- and mid-latitudes. Although the CTIPe N_{max} overestimated the GOLD N_{max} , both showed similar seasonal and latitudinal variations. It is worth noting that N_{max} also fluctuates significantly during periods of low solar activity. The GOLD observations revealed significant temporal and spatial phenomena, including fluctuations at low solar activity confirming the role of EUV in the equatorial region, a winter anomaly, and an increase in N_{max} with solar activity. We investigate the relationship between N_{max} and the solar proxies (Q_{EUV} , EUV, and F10.7). The results show that the correlation coefficients between GOLD N_{max} and the solar proxies are higher than for CTIPe N_{max} ; however, the overall correlation is low $\approx 0.55(0.30)$.

for GOLD Nmax (CTIpe Nmax) with EUV. The low correlation could be due to dominant external forcings such as lower atmospheric forcings, and geomagnetic activity (e.g., Cai et al., 2021; Forbes et al., 2000; Vaishnav et al., 2019).

Recently, Cai et al. (2021) showed that the geomagnetic forcing during geomagnetically quiet periods in the solar minimum could sometimes play an important role in generating variations of the TI composition at the mid-latitudes. Therefore, we further investigated the correlation during the medium-term (27-day solar variations) and long-term (averaging 81 days) ionospheric response using GOLD Nmax, solar proxies (Q_{EUV} and F10.7 index), and geomagnetic activity. Through correlation analysis, it was found that the correlation coefficients (between solar activity proxies and Nmax) were larger for the long-term response, followed by the medium-term response. The study indicates also a high correlation between geomagnetic activity and Nmax for medium-term ionospheric responses. The GOLD Nmax correlates well with the Q_{EUV} compared to F10.7 at longer timescale. Furthermore, a low correlation between nighttime Nmax and solar proxies (Q_{EUV} and F10.7) was observed in the equatorial region (see Figure 5).

We compared the O_2 density profiles obtained from GOLD with those simulated by the model. Our results show that the model agreed better in the Northern Hemisphere than in the Southern Hemisphere. Furthermore, we observed that the O_2 density from the GOLD data is generally lower than the modeled density, consistent with previous findings (e.g., Lumpe et al., 2020).

We observed differences in the magnitudes of GOLD O/N_2 compared to GUVI and CTIpe O/N_2 . GOLD O/N_2 was higher and more variable than CTIpe O/N_2 at low and mid-latitudes. However, the seasonal and annual variations of CTIpe O/N_2 are similar to those of GOLD O/N_2 as Qian et al. (2022), who found that the GOLD O/N_2 is higher than GUVI and NRLMSISE-00 O/N_2 . The seasonal variations in O/N_2 could be related to seasonal variations in geomagnetic activity and mean circulation (Martinez & Lu, 2023).

Cross-correlation analysis of IGS and CTIpe TEC with solar proxies indicates low correlation during low solar activity. The correlation in the equatorial region is stronger in the case of TEC, to which the equatorial ionization anomaly also contributes (Figure 9). Comparing with Figure 5, the spatial pattern of TEC, the Nmax exhibits low correlation. This could be attributed to the fact that TEC is vertically integrated and less affected by the plasma movement in the equatorial region (Lee et al., 2012).

Furthermore, the delayed ionospheric response against solar flux was studied using IGS and CTIpe TEC during the 27-day solar rotation at 80°W longitude. The delayed response is estimated to be less than one day (about 15 hr for IGS TEC and 16 hr for CTIpe TEC). The results also show the latitudinal variations of the delayed response, which may be caused by the compositional (O/N_2) and thermospheric circulation changes. The analysis suggests that O/N_2 is positively correlated with solar flux in the Northern Hemisphere (25°N–55°N), suggesting that O/N_2 can affect the delayed ionospheric response. Whereas, a negative correlation at other latitudes indicates the possible role of other factors, like geomagnetic activity and lower atmospheric forcing.

In this study, we presented and discussed the TI response to solar irradiance variations using measurements from the GOLD mission, GUVI and those simulated by the CTIpe model during the solar minimum of SC 25, 2019 to 2021. The main results may be summarized as follows:

- GOLD observations and model simulations show significant differences in TI parameters (Nmax, O/N_2 , and O_2) depending on season, latitude, and time.
- Seasonal and latitudinal patterns were clearly identified in O/N_2 and Nmax, consistent in both observations and model simulations.
- A higher correlation was found between Q_{EUV} and both IGS TEC and GOLD Nmax. However, the correlation between CTIpe simulated TEC and Nmax and Q_{EUV} is weak. This implies that F10.7 for solar flux could also be a factor that leads to inadequate modeling of TEC.
- The analysis of O/N_2 ratio in correlation with solar activity reveals its impact on the delayed ionospheric response in the mid-latitude Northern Hemisphere.

This study was conducted during a period of low solar activity, as it relied on GOLD observations from 2019 to 2021. However, further research is needed to understand how the ionosphere responds during high solar activity.

Conflict of Interest

The authors declare no conflicts of interest relevant to this study.

Data Availability Statement

IGS TEC maps can be downloaded from http://cdis.nasa.gov/Data_and_Derived_Products/GNSS/atmospheric_products.html (NASA, 2022a). GOLD O/N_2 , Q_{EUV} , N_{max} , and O_2 can be downloaded from <http://gold.cs.ucf.edu/search/> (NASA, 2022b). Daily Kp indices have been downloaded from <https://omniweb.gsfc.nasa.gov/form/dx1.html> (NASA, 2022d). The F10.7 index at 1 AU have been obtained from the LISIRD database (LASP, 2022, <https://lasp.colorado.edu/lisird/>). GUVI O/N_2 data are available at: <http://guvitimed.jhuapl.edu/data/products> (NASA, 2022e). The CTIPE simulation data used for this work can be accessed at <https://doi.org/10.5281/zenodo.8145356> (Vaishnav, 2023).

Acknowledgments

The study has been supported by Deutsche Forschungsgemeinschaft (DFG) through Grants JA 836/48-1 and SCHM 3761/1-1. Open Access funding enabled and organized by Projekt DEAL.

References

- Afraimovich, E. L., Astafeyeva, E. I., Oinats, A. V., Yasukevich, Y. V., & Zhivetiev, I. V. (2008). Global electron content: A new conception to track solar activity. *Annales Geophysicae*, 26(2), 335–344. <https://doi.org/10.5194/angeo-26-335-2008>
- Altadill, D., & Apostolov, E. (2003). Time and scale size of planetary wave signatures in the ionospheric F region: Role of the geomagnetic activity and mesosphere/lower thermosphere winds. *Journal of Geophysical Research*, 108(A11), 1403. <https://doi.org/10.1029/2003JA010015>
- Appleton, E. V. (1946). Two anomalies in the ionosphere. *Nature*, 157(3995), 691. <https://doi.org/10.1038/157691a0>
- BenMoussa, A., Giordanengo, B., Gissot, S., Dammasch, I. E., Dominique, M., Hochedez, J.-F., et al. (2015). Degradation assessment of LYRA after 5 years on orbit—Technology demonstration. *Experimental Astronomy*, 39(1), 29–43. <https://doi.org/10.1007/s10686-014-9437-7>
- Cai, X., Burns, A. G., Wang, W., Qian, L., Solomon, S. C., Eastes, R. W., et al. (2021). Investigation of a neutral “Tongue” observed by GOLD during the geomagnetic storm on May 11, 2019. *Journal of Geophysical Research: Space Physics*, 126(6), e2020JA028817. <https://doi.org/10.1029/2020ja028817>
- Christensen, A. B., Paxton, L. J., Avery, S., Craven, J., Crowley, G., Humm, D. C., et al. (2003). Initial observations with the global ultraviolet imager (GUVI) in the NASA TIMED satellite mission. *Journal of Geophysical Research*, 108(A12), 1451. <https://doi.org/10.1029/2003ja009918>
- Codrescu, M. V., Fuller-Rowell, T. J., Munteanu, V., Minter, C. F., & Millward, G. H. (2008). Validation of the coupled thermosphere ionosphere plasmasphere electrodynamic model: CTIPE-mass spectrometer incoherent scatter temperature comparison. *Space Weather*, 6(9). <https://doi.org/10.1029/2007sw000364>
- Codrescu, M. V., Negrea, C., Fedrizzi, M., Fuller-Rowell, T. J., Dobin, A., Jakowsky, N., et al. (2012). A real-time run of the coupled thermosphere ionosphere plasmasphere electrodynamic (CTIPE) model. *Space Weather*, 10(2). <https://doi.org/10.1029/2011sw000736>
- Correia, J., Evans, J. S., Lumpe, J. D., Krywonos, A., Daniell, R., Veibell, V., et al. (2021). Thermospheric composition and solar EUV flux from the global-scale observations of the limb and disk (GOLD) mission. *Journal of Geophysical Research: Space Physics*, 126(12), e2021JA029517. <https://doi.org/10.1029/2021ja029517>
- Dudok de Wit, T., Kretschmar, M., Lilienstein, J., & Woods, T. (2009). Finding the best proxies for the solar UV irradiance. *Geophysical Research Letters*, 36(10), 2–5. <https://doi.org/10.1029/2009GL037825>
- Eastes, R. W., McClintock, W. E., Burns, A. G., Anderson, D. N., Andersson, L., Aryal, S., et al. (2020). Initial observations by the GOLD mission. *Journal of Geophysical Research: Space Physics*, 125(7), e2020JA027823. <https://doi.org/10.1029/2020ja027823>
- Eastes, R. W., McClintock, W. E., Burns, A. G., Anderson, D. N., Andersson, L., Codrescu, M., et al. (2017). The global-scale observations of the limb and disk (GOLD) mission. *Space Science Reviews*, 212(1–2), 383–408. <https://doi.org/10.1007/s11214-017-0392-2>
- Fang, T.-W., Akmaev, R., Fuller-Rowell, T., Wu, F., Maruyama, N., & Millward, G. (2013). Longitudinal and day-to-day variability in the ionosphere from lower atmosphere tidal forcing. *Geophysical Research Letters*, 40(11), 2523–2528. <https://doi.org/10.1002/grl.50550>
- Forbes, J. M., Palo, S. E., & Zhang, X. (2000). Variability of the ionosphere. *Journal of Atmospheric and Solar-Terrestrial Physics*, 62(8), 685–693. [https://doi.org/10.1016/S1364-6826\(00\)00029-8](https://doi.org/10.1016/S1364-6826(00)00029-8)
- Fuller-Rowell, T. J., & Rees, D. (1983). Derivation of a conservation equation for mean molecular weight for a two-constituent gas within a three-dimensional, time-dependent model of the thermosphere. *Planetary and Space Science*, 31(10), 1209–1222. [https://doi.org/10.1016/0032-0633\(83\)90112-5](https://doi.org/10.1016/0032-0633(83)90112-5)
- Gan, Q., Eastes, R. W., Burns, A. G., Wang, W., Qian, L., Solomon, S. C., et al. (2020). New observations of large-scale waves coupling with the ionosphere made by the GOLD mission: Quasi-16-day wave signatures in the F-region OI 135.6-nm nightglow during sudden stratospheric warmings. *Journal of Geophysical Research: Space Physics*, 125(4), e2020JA027880. <https://doi.org/10.1029/2020ja027880>
- Hernández-Pajares, M., Juan, J. M., Sanz, J., Orus, R., Garcia-Rigo, A., Feltens, J., et al. (2009). The IGS VTEC maps: A reliable source of ionospheric information since 1998. *Journal of Geodesy*, 83(3–4), 263–275. <https://doi.org/10.1007/s00190-008-0266-1>
- Jacobi, C., Jakowski, N., Schmidtke, G., & Woods, T. N. (2016). Delayed response of the global total electron content to solar EUV variations. *Advances in Radio Science*, 14, 175–180. <https://doi.org/10.5194/ars-14-175-2016>
- Jakowski, N., Fichtelmann, B., & Jungstand, A. (1991). Solar activity control of ionospheric and thermospheric processes. *Journal of Atmospheric and Terrestrial Physics*, 53(11–12), 1125–1130. [https://doi.org/10.1016/0021-9169\(91\)90061-b](https://doi.org/10.1016/0021-9169(91)90061-b)
- Jakowski, N., Hoque, M. M., Kriegl, M., & Patidar, V. (2015). The persistence of the NWA effect during the low solar activity period 2007–2009. *Journal of Geophysical Research: Space Physics*, 120(10), 9148–9160. <https://doi.org/10.1002/2015ja021600>
- Judge, D. L., McMullin, D. R., Ogawa, H. S., Hovestadt, D., Klecker, B., Hilchenbach, M., et al. (1998). First solar EUV irradiances obtained from SOHO by the SEM. *Solar Physics*, 177(1/2), 161–173. <https://doi.org/10.1023/a:1004929011427>
- Kutiev, I., Tsagouri, I., Perrone, L., Pancheva, D., Mukhtarov, P., Mikhailov, A., et al. (2013). Solar activity impact on the Earth's upper atmosphere. *Journal of Space Weather and Space Climate*, 3, A06. <https://doi.org/10.1051/swsc/2013028>
- LASP (2022). *LASP interactive solar irradiance data center*. University of Colorado. Retrieved from <https://lasp.colorado.edu/lisird/>
- Laštovička, J. (2021). Long-term trends in the upper atmosphere. In W. Wang, Y. Zhang, & L. J. Paxton (Eds.), *Upper atmosphere dynamics and energetics*. <https://doi.org/10.1002/9781119815631.ch17>
- Lean, J. L., White, O. R., Livingston, W. C., & Picone, J. M. (2001). Variability of a composite chromospheric irradiance index during the 11-year activity cycle and over longer time periods. *Journal of Geophysical Research*, 106(A6), 10645–10658. <https://doi.org/10.1029/2000ja000340>
- Lee, C.-K., Han, S.-C., Bilitza, D., & Seo, K.-W. (2012). Global characteristics of the correlation and time lag between solar and ionospheric parameters in the 27-day period. *Journal of Atmospheric and Solar-Terrestrial Physics*, 77, 219–224. <https://doi.org/10.1016/j.jastp.2012.01.010>
- Lin, C. H., Liu, J. Y., Fang, T. W., Chang, P. Y., Tsai, H. F., Chen, C. H., & Hsiao, C. C. (2007). Motions of the equatorial ionization anomaly crests imaged by FORMOSAT-3/COSMIC. *Geophysical Research Letters*, 34(19), L19101. <https://doi.org/10.1029/2007gl030741>

- Luan, X., Wang, W., Burns, A., & Dou, X. (2017). Solar cycle variations of thermospheric O/N_2 longitudinal pattern from TIMED/GUVI. *Journal of Geophysical Research: Space Physics*, 122(2), 2605–2618. <https://doi.org/10.1002/2016JA023696>
- Lumpe, J. D., Bevilacqua, R. M., Hoppel, K. W., & Randall, C. E. (2002). POAM III retrieval algorithm and error analysis. *Journal of Geophysical Research*, 107(D21), ACH5–1–ACH5–32. <https://doi.org/10.1029/2002jd002137>
- Lumpe, J. D., McClintock, W. E., Evans, J. S., Correia, J., Veibell, V., Beland, S., & Eastes, R. (2020). A new data set of thermospheric molecular oxygen from the global-scale observations of the limb and disk (GOLD) mission. *Journal of Geophysical Research: Space Physics*, 125(4), e2020JA027812. <https://doi.org/10.1029/2020ja027812>
- Ma, R., Xu, J., Wang, W., & Lei, J. (2012). The effect of ~27 day solar rotation on ionospheric F2 region peak densities (NmF2). *Journal of Geophysical Research*, 117(A3), A03303. <https://doi.org/10.1029/2011ja017190>
- Martinez, B. C., & Lu, X. (2023). Quantifying day-to-day variability of O/N_2 and its correlation with geomagnetic activity using GOLD. *Frontiers in Astronomy and Space Sciences*, 10, 1129279. <https://doi.org/10.3389/fspas.2023.1129279>
- Min, K., Park, J., Kim, H., Kim, V., Kil, H., Lee, J., et al. (2009). The 27-day modulation of the low-latitude ionosphere during a solar maximum. *Journal of Geophysical Research*, 114(4), 1–8. <https://doi.org/10.1029/2008JA013881>
- NASA. (2022a). GNSS atmospheric products. Retrieved from http://cdsis.nasa.gov/Data_and_Derived_Products/GNSS/atmospheric_products.html
- NASA. (2022b). GOLD science data products. Retrieved from <http://gold.cs.ucf.edu/search/>
- NASA. (2022c). *GOLD science data products guide—rev 3.0*. NASA/Goddard Space Flight Center. Retrieved from https://gold.cs.ucf.edu/wp-content/documentation/GOLD_Public_Science_Data_Products_Guide_Rev3.0.pdf
- NASA. (2022d). NASA/GSFC's OMNIWeb interface. Retrieved from <https://omniweb.gsfc.nasa.gov/form/dx1.html>
- NASA. (2022e). TIMED GUVI observations. Retrieved from <http://guvitimed.jhuapl.edu/data/products>
- Oberheide, J., Pedatella, N. M., Gan, Q., Kumari, K., Burns, A. G., & Eastes, R. W. (2020). Thermospheric composition O/N_2 response to an altered meridional mean circulation during sudden stratospheric warmings observed by GOLD. *Geophysical Research Letters*, 47(1), e2019GL086313. <https://doi.org/10.1029/2019gl086313>
- Qian, L., Burns, A. G., Solomon, S. C., & Wang, W. (2013). Annual/semiannual variation of the ionosphere. *Geophysical Research Letters*, 40(10), 1928–1933. <https://doi.org/10.1002/grl.50448>
- Qian, L., Gan, Q., Wang, W., Cai, X., Eastes, R., & Yue, J. (2022). Seasonal variation of thermospheric composition observed by NASA GOLD. *Journal of Geophysical Research: Space Physics*, 127(6), e2022JA030496. <https://doi.org/10.1029/2022ja030496>
- Qian, L., Solomon, S. C., & Kane, T. J. (2009). Seasonal variation of thermospheric density and composition. *Journal of Geophysical Research*, 114(A1), A01312. <https://doi.org/10.1029/2008ja013643>
- Ren, D., Lei, J., Wang, W., Burns, A., Luan, X., & Dou, X. (2018). Does the peak response of the ionospheric F2 region plasma lag the peak of 27-day solar flux variation by multiple days? *Journal of Geophysical Research: Space Physics*, 123(9), 7906–7916. <https://doi.org/10.1029/2018ja025835>
- Ren, D., Lei, J., Wang, W., Burns, A., Luan, X., & Dou, X. (2019). A simulation study on the time delay of daytime thermospheric temperature response to the 27-day solar EUV flux variation. *Journal of Geophysical Research: Space Physics*, 124(11), 9184–9193. <https://doi.org/10.1029/2019ja027000>
- Ren, D., Lei, J., Wang, W., Burns, A., Luan, X., & Dou, X. (2020). Different peak response time of daytime thermospheric neutral species to the 27-day solar EUV flux variations. *Journal of Geophysical Research: Space Physics*, 125(7), e2020JA027840. <https://doi.org/10.1029/2020ja027840>
- Richards, P. (2001). Seasonal and solar cycle variations of the ionospheric peak electron density: Comparison of measurement and models. *Journal of Geophysical Research*, 106(A7), 12803–12819. <https://doi.org/10.1029/2000JA000365>
- Rishbeth, H. (1998). How the thermospheric circulation affects the ionospheric F2 layer. *Journal of Atmospheric and Solar-Terrestrial Physics*, 60(14), 1385–1402. [https://doi.org/10.1016/s1364-6826\(98\)00062-5](https://doi.org/10.1016/s1364-6826(98)00062-5)
- Rishbeth, H., & Mendillo, M. (2001). Patterns of F2-layer variability. *Journal of Atmospheric and Solar-Terrestrial Physics*, 63(15), 1661–1680. [https://doi.org/10.1016/s1364-6826\(01\)00036-0](https://doi.org/10.1016/s1364-6826(01)00036-0)
- Schmölter, E., Berdermann, J., & Codrescu, M. (2021). The delayed ionospheric response to the 27-day solar rotation period analyzed with GOLD and IGS TEC data. *Journal of Geophysical Research: Space Physics*, 126(2), e2020JA028861. <https://doi.org/10.1029/2020ja028861>
- Schmölter, E., Berdermann, J., Jakowski, N., & Jacobi, C. (2020). Spatial and seasonal effects on the delayed ionospheric response to solar EUV changes. *Annales Geophysicae*, 38(1), 149–162. <https://doi.org/10.5194/angeo-38-149-2020>
- Schmölter, E., Berdermann, J., Jakowski, N., Jacobi, C., & Vaishnav, R. (2018). Delayed response of the ionosphere to solar EUV variability. *Advances in Radio Science*, 16, 149–155. <https://doi.org/10.5194/ars-16-149-2018>
- Schmölter, E., Heymann, F., Savigny, C., & Berdermann, J. (2022). The height-dependent delayed ionospheric response to solar EUV. *Journal of Geophysical Research: Space Physics*, 127(3), e2021JA030118. <https://doi.org/10.1029/2021ja030118>
- Schmölter, E., & von Savigny, C. (2022). Solar activity driven 27-day signatures in ionospheric electron and molecular oxygen densities. *Journal of Geophysical Research: Space Physics*, 127(9). <https://doi.org/10.1029/2022ja030671>
- Schunk, R., & Nagy, A. (2009). *Ionospheres: Physics, plasma physics, and chemistry*. Cambridge university press.
- Strickland, D. J., Evans, J. S., & Paxton, L. J. (1995). Satellite remote sensing of thermospheric O/N_2 and solar EUV: 1. Theory. *Journal of Geophysical Research*, 100(A7), 12217–12226. <https://doi.org/10.1029/95ja00574>
- Strickland, D. J., Lean, J. L., Daniell, R. E., Knight, H. K., Woo, W. K., Meier, R. R., et al. (2007). Constraining and validating the Oct/Nov 2003 X-class EUV flare enhancements with observations of FUV dayglow and E-region electron densities. *Journal of Geophysical Research*, 112(A6), A06313. <https://doi.org/10.1029/2006ja012074>
- Tapping, K. F. (2013). The 10.7 cm solar radio flux (F10.7). *Space Weather*, 11(7), 394–406. <https://doi.org/10.1002/swe.20064>
- Tsurutani, B., Verkhoglyadova, O., Mannucci, A., Lakhina, G., Li, G., & Zank, G. (2009). A brief review of “solar flare effects” on the ionosphere. *Radio Science*, 44(01), 1–14. <https://doi.org/10.1029/2008RS004029>
- Vaishnav, R. (2023). *CTIpe model simulations*. Zenodo. <https://doi.org/10.5281/zenodo.8145356>
- Vaishnav, R., Jacobi, C., & Berdermann, J. (2019). Long-term trends in the ionospheric response to solar extreme-ultraviolet variations. *Annales Geophysicae*, 37(6), 1141–1159. <https://doi.org/10.5194/angeo-37-1141-2019>
- Vaishnav, R., Jacobi, C., Berdermann, J., Codrescu, M., & Schmölter, E. (2021). Role of eddy diffusion in the delayed ionospheric response to solar flux changes. *Annales Geophysicae*, 39(4), 641–655. <https://doi.org/10.5194/angeo-39-641-2021>
- Vaishnav, R., Jacobi, C., Berdermann, J., Schmölter, E., & Codrescu, M. (2018). Ionospheric response to solar EUV variations: Preliminary results. *Advances in Radio Science*, 16, 157–165. <https://doi.org/10.5194/ars-16-157-2018>
- Vaishnav, R., Jacobi, C., Berdermann, J., Schmölter, E., & Codrescu, M. (2022). Delayed ionospheric response to solar extreme ultraviolet radiation variations: A modeling approach. *Advances in Space Research*, 69(6), 2460–2476. <https://doi.org/10.1016/j.asr.2021.12.041>

- Vaishnav, R., Schmölter, E., Jacobi, C., Berdermann, J., & Codrescu, M. (2021). Ionospheric response to solar extreme ultraviolet radiation variations: Comparison based on CTIPe model simulations and satellite measurements. *Annales Geophysicae*, 39(2), 341–355. <https://doi.org/10.5194/angeo-39-341-2021>
- Woods, T. N., Eparvier, F. G., Bailey, S. M., Chamberlin, P. C., Lean, J., Rottman, G. J., et al. (2005). Solar EUV Experiment (SEE): Mission overview and first results. *Journal of Geophysical Research*, 110(A1), A01312. <https://doi.org/10.1029/2004ja010765>
- Woods, T. N., & Rottman, G. J. (2002). Solar ultraviolet variability over time periods of aeronomic interest. In *Atmospheres in the solar system: Comparative aeronomy* (pp. 221–233). <https://doi.org/10.1029/130gm14>
- Zhang, Y., & Paxton, L. J. (2011). Long-term variation in the thermosphere: TIMED/GUVI observations. *Journal of Geophysical Research*, 116(A2), A00H02. <https://doi.org/10.1029/2010ja016337>
- Zhang, Y., Paxton, L. J., Morrison, D., Wolven, B., Kil, H., Meng, C., et al. (2004). O/N_2 changes during 1–4 October 2002 storms: IMAGE SI-13 and TIMED/GUVI observations. *Journal of Geophysical Research*, 109(A10), A10308. <https://doi.org/10.1029/2004ja010441>